

ON THE NORMALIZATION OF THE COSMIC STAR FORMATION HISTORY

ANDREW M. HOPKINS¹ AND JOHN F. BEACOM^{2,3}

Received 2006 January 16; accepted 2006 June 12

ABSTRACT

Strong constraints on the cosmic star formation history (SFH) have recently been established using ultraviolet and far-infrared measurements, refining the results of numerous measurements over the past decade. The data show a compellingly consistent picture of the SFH out to redshift $z \approx 6$, with especially tight constraints for $z \lesssim 1$. We fit these data with simple analytical forms and derive conservative uncertainties. Since the $z \lesssim 1$ SFH data are quite precise, we investigate the sequence of assumptions and corrections that together affect the SFH normalization to test their accuracy, both in this redshift range and beyond. As lower limits on this normalization, we consider the evolution in stellar and metal mass densities, and supernova rate density, finding it unlikely that the SFH normalization is much lower than indicated by our direct fit. As a corresponding upper limit on the SFH normalization, we consider the Super-Kamiokande limit on the electron antineutrino ($\bar{\nu}_e$) flux from past core-collapse supernovae, which applies primarily to $z \lesssim 1$. We find consistency with the SFH only if the neutrino temperatures from supernova events are relatively modest. Constraints on the assumed initial mass function (IMF) also become apparent. The traditional Salpeter IMF, assumed for convenience by many authors, is known to be a poor representation at low stellar masses ($\lesssim 1 M_\odot$), and we show that recently favored IMFs are also constrained. In particular, somewhat shallow, or top-heavy, IMFs may be preferred, although they cannot be too top-heavy. To resolve the outstanding issues, improved data are called for on the supernova rate density evolution, the ranges of stellar masses leading to core-collapse and type Ia supernovae, and the antineutrino and neutrino backgrounds from core-collapse supernovae.

Subject headings: galaxies: evolution — galaxies: formation — galaxies: starburst — neutrinos — supernovae: general

1. INTRODUCTION

In the past few years, measurement of the evolution of galaxy luminosity functions at a broad range of wavelengths has rapidly matured. One consequence of this has been the refinement in our understanding of how the space density of the galaxy star formation rate (SFR) evolves (Lilly et al. 1996; Madau et al. 1996). In particular, the recent results from the Sloan Digital Sky Survey (SDSS), the *Galaxy Evolution Explorer* (GALEX), the Classifying Objects by Medium-Band Observations in 17 Filters survey (COMBO17) at ultraviolet (UV) wavelengths, and the *Spitzer Space Telescope* at far-infrared (FIR) wavelengths now allow this cosmic star formation history (SFH) to be quite tightly constrained (to within $\approx 30\%$ – 50%) up to redshifts of $z \approx 1$. Combined with measurements of the SFH at higher redshifts from the FIR, submillimeter, Balmer line, and UV emission, the SFH is reasonably well determined (within a factor of ~ 3 at $z \gtrsim 1$) up to $z \approx 6$ (e.g., Hopkins 2004).

Additional results from the Super-Kamiokande (SK) particle detector provide a strong limit on the electron antineutrino ($\bar{\nu}_e$) flux, $1.2 \text{ cm}^{-2} \text{ s}^{-1}$ (for $E_\nu > 19.3 \text{ MeV}$), originating from supernova Type II (SN II; here and throughout, we assume the inclusion of all core-collapse supernovae: Types II, Ib, and Ic) events associated with the SFH (Malek et al. 2003). This limit on the diffuse supernova neutrino background (DSNB) acts to constrain the normalization of the SFH (Fukugita & Kawasaki 2003; Ando 2004; Strigari et al. 2004, 2005). An exploration of quantities predicted from the SFH, the stellar and metal mass density evo-

lution, and supernova (SN) rate evolution, provides further insight into the allowable normalization of the SFH (Strigari et al. 2005). This series of interconnected physical properties of galaxies and SNe provides an emerging opportunity for determining the level of the SFH normalization; and the SFH measurements, particularly for $z \lesssim 1$, now have the precision to allow this exploration of their accuracy. Constraining the normalization of the SFH will support a range of quantitative analyses of galaxy evolution, including the mass dependence of the SFH (e.g., Papovich et al. 2006; Juneau et al. 2005; Heavens et al. 2004) and the reasons underlying the decline in the SFH to low redshifts (e.g., Bell et al. 2005).

The sequence of assumptions explored here starts from observed luminosity density measurements. (1) To these measurements, dust corrections (where necessary), SFR calibrations, and IMF assumptions are applied to produce corrected SFH measurements. (2) From the SFH, assumptions about the high-mass IMF fraction that produces SNe II lead to predictions for the SN II rate density. This can be compared directly with measurements of this quantity. (3) Assumptions about the neutrino emission of SNe II then give a prediction of the DSNB for comparison with the SK limit. Since optical SNe II can be hidden from observations by dust obscuration, the present SN II rate density measurements may merely be lower limits. In contrast, since neutrinos are unaffected by dust, the DSNB provides an absolute upper limit on the true SN II rate. The consistency that we find between the SFH data and the SK upper limit on the DSNB indicates that there is little room to increase the overall normalization of the SFH. Thus, this constrains each of the dust corrections, the assumed IMF, and the neutrino emission per supernova. None can be increased significantly without requiring at least one of the others to be reduced below its expected range. Below, we focus especially on the assumed IMF, noting the more detailed treatment of the neutrino emission per supernova by Yüksel

¹ School of Physics, University of Sydney, NSW 2006, Australia; ahopkins@physics.usyd.edu.au.

² Department of Physics, The Ohio State University, 191 West Woodruff Avenue, Columbus, OH 43210; beacom@mps.ohio-state.edu.

³ Department of Astronomy, The Ohio State University, 140 West 18th Avenue, Columbus, OH 43210.

et al. (2006). A parallel set of assumptions to step (2) regarding the generation of SNe Ia lead to predictions for the SN Ia rate density, and this is explored in some detail with tantalizing implications regarding the extent of the SN Ia delay time.

In § 2 we update the SFH data compilation of Hopkins (2004) and address some of the assumptions that affect the normalization. We identify the best parametric fit to the most robust subset of this data in § 3, consistent with the $\overline{\tau}_e$ limits from SK. In § 4 we present the results of this fitting in terms of the stellar and metal mass density evolution and the SN II and SN Ia rate evolution. The implications for the assumed IMF and SN Ia properties are discussed further in § 5.

The 737 cosmology⁴ is assumed throughout, with $H_0 = 70 \text{ km s}^{-1} \text{ Mpc}^{-1}$, $\Omega_M = 0.3$, and $\Omega_\Lambda = 0.7$ (e.g., Spergel et al. 2003).

2. THE DATA

The compilation of Hopkins (2004) was taken as the starting point for this analysis, shown in Figure 1 as gray points. These data are reproduced from Figure 1 of Hopkins (2004) and use their “common” obscuration correction where necessary. Additional measurements are indicated in color in Figure 1. For $z \lesssim 3$, these consist of FIR ($24 \mu\text{m}$) photometry from the *Spitzer Space Telescope* (Pérez-González et al. 2005; Le Flo’c’h et al. 2005) and UV measurements from the SDSS (Baldry et al. 2005), *GALEX* (Arnouts et al. 2005; Schiminovich 2005), and the COMBO17 project (Wolf et al. 2003). At $z = 0.05$, a new radio (1.4 GHz) measurement is shown (Mauch 2005), which is highly consistent with the FIR results, as expected from the radio-FIR correlation (Bell 2003a). Also at low redshift ($z = 0.01$) is a new $H\alpha$ -derived measurement (Hanish et al. 2006). At higher redshifts, additional SFH measurements come from the Hubble Ultra Deep Field (UDF; Thompson et al. 2006) and from various photometric dropout analyses, probing rest-frame UV luminosities (Bouwens et al. 2003a, 2003b, 2006; Ouchi et al. 2004; Bunker et al. 2004). The UDF measurements of Thompson et al. (2006) are derived through fitting spectral energy distributions to the UDF photometry using a variety of templates with a range of underlying assumptions. In particular, this includes different IMF assumptions for different templates. Although we show these measurements in Figure 1 for illustrative purposes (having scaled them, assuming they were uniformly estimated using a Salpeter 1955 IMF), we do not include them in subsequent analyses, as there is no clear process for scaling these measurements to our assumed IMFs in the absence of a common original IMF assumption.

2.1. SFR Calibrations

Throughout we assume the same SFR calibrations as Hopkins (2004). Uncertainties in the calibrations for different SFR indicators will correspond to uncertainties in the resulting SFH normalization for that indicator. Issues regarding SFR calibrations are detailed in Moustakas et al. (2006), Kennicutt (1998), and Condon (1992). Perhaps the most uncertain calibrations are the radio (1.4 GHz) and FIR indicators (although the $[\text{O II}]$ indicator has a similar level of uncertainty). For FIR SFRs, Kennicutt (1998) indicates a variation of about 30% between calibrations in the literature. Bell (2003a) refines the 1.4 GHz calibration of Condon (1992), following an exploration of the origins of the radio-FIR correlation, and the implication is that the radio SFR calibration has about the same uncertainty as the FIR, assuming

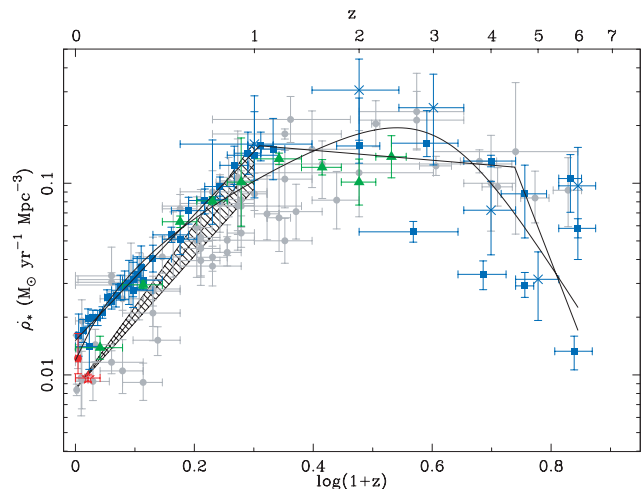


FIG. 1.— Evolution of SFR density with redshift. Data shown here have been scaled, assuming the SalA IMF. The gray points are from the compilation of Hopkins (2004). The hatched region is the FIR ($24 \mu\text{m}$) SFH from Le Flo’c’h et al. (2005). The green triangles are FIR ($24 \mu\text{m}$) data from Pérez-González et al. (2005). The open red star at $z = 0.05$ is based on radio (1.4 GHz) data from Mauch (2005). The filled red circle at $z = 0.01$ is the $H\alpha$ estimate from Hanish et al. (2006). The blue squares are UV data from Baldry et al. (2005), Wolf et al. (2003), Arnouts et al. (2005), Bouwens et al. (2003a, 2003b, 2005a), Bunker et al. (2004), and Ouchi et al. (2004). The blue crosses are the UDF estimates from Thompson et al. (2006). Note that these have been scaled to the SalA IMF, assuming they were originally estimated using a uniform Salpeter (1955) IMF. The solid lines are the best-fitting parametric forms (see text for details of which data are used in the fitting). Although the FIR SFH of Le Flo’c’h et al. (2005) is not used directly in the fitting, it has been used to effectively obscuration-correct the UV data to the values shown, which are used in the fitting. Note that the top logarithmic scale is labeled with redshift values, not $(1+z)$.

no contamination by emission from an active galactic nucleus (AGN). More significantly, however, for individual galaxies there can be large differences, up to an order of magnitude, in the SFRs inferred through different indicators (e.g., Hopkins et al. 2003), although on average for large samples there is a high level of consistency. This is reflected in the overall consistency between SFR densities, $\dot{\rho}_*$, estimated from different indicators, with at most about a factor of 2 or 3 variation (which also includes the uncertainty in dust obscuration corrections, where relevant). This scatter is still notably larger than the uncertainties in individual SFR calibrations and is suggestive of the overall level of systematic uncertainty in the individual calibrations. It is likely that this reflects subtleties such as low-level AGN contamination in various samples, the difficulties with aperture corrections where necessary, dust obscuration uncertainties (discussed further below), and other issues. It is for these reasons that we neglect the details of the underlying SFR calibrations, as their small formal uncertainties are dominated by these larger systematics. Furthermore, the effect of these systematics between different SFR indicators acts to increase the scatter in the overall SFH compilation, rather than to systematically shift all measurements in a common direction. So even the factor of 2–3 variation here cannot be viewed precisely as an uncertainty on the SFH normalization. In this sense, the level of consistency between $\dot{\rho}_*$ measurements using dramatically different samples and SFR indicators, over the whole redshift range up to $z \approx 6$, is actually quite encouraging.

2.2. Dust Obscuration Corrections

The issue of dust corrections is complex and has been addressed by many authors (e.g., Buat et al. 2002, 2005; Bell 2003b; Calzetti 2001). Hopkins (2004) compared assumptions

⁴ Thanks to Sandhya Rao (Rao et al. 2006) for this terminology.

of a “common” obscuration correction to a luminosity-dependent correction on the SFH. The latter leads, for UV and emission-line estimators, to somewhat higher values for $\dot{\rho}_*$ at higher redshift, although both methods give results essentially consistent with SFH estimators unaffected by obscuration. Bell (2003a) shows that SFRs derived from summing total-IR (8–1000 μm) and UV indicators using the SFR calibrations of Kennicutt (1998) adopted here are consistent within a factor of 2 with obscuration-corrected $\text{H}\alpha$ SFRs. This technique, suggested as the preferred method by Iglesias-Paramo et al. (2006), has the strong advantage that it avoids assumptions about the extent or form of the obscuration and variations due to possible luminosity bias in the UV selected sample (e.g., Hopkins et al. 2001; Sullivan et al. 2001; Afonso et al. 2003).

To implement effective obscuration corrections for the UV measurements at $z \lesssim 1$ (Baldry et al. 2005; Wolf et al. 2003; Arnouts et al. 2005), we thus take advantage of the well-established FIR SFR densities up to $z = 1$ from Le Floc’h et al. (2005). The UV data at $z \leq 1$ are “obscuration corrected” by adding the FIR SFR density from Le Floc’h et al. (2005) to each point. As shown by Bell (2003a) for individual systems, this technique results in $\dot{\rho}_*$ estimates consistent with the obscuration-corrected $\text{H}\alpha$ measurements, in particular the recent estimates from Hanish et al. (2006) and Doherty et al. (2006; also compare our Fig. 1 to Fig. 1 of Hopkins 2004). This result is consistent with the interpretation of Takeuchi et al. (2005) that about half the SFR density in the local universe is obscured by dust (see also Martin et al. 2005), increasing to about 80% by $z \approx 1$, a trend that can be seen in the different slopes of the (obscuration-corrected) UV measurements and FIR measurements in Figure 1. For obscuration corrections to the UV data between $1 < z < 3$, we rely on the fact that the FIR measurements of Pérez-González et al. (2005) are quite flat in this domain, as well as being highly consistent with those of Le Floc’h et al. (2005) at $z < 1$ and add the constant SFR density corresponding to that of Le Floc’h et al. (2005) at $z = 1$. This is also consistent with the recent measurements of obscuration corrections for UV luminosities at $z \approx 2$ by Erb et al. (2006), who find a typical correction factor of ≈ 4.5 . At higher redshifts, we apply a “common” obscuration correction to the UV data as detailed in Hopkins (2004). The reliability of this assumption is open to question but may not be unreasonable, as a comparison with the measured color excesses of Ouchi et al. (2004) illustrates. The obscuration-corrected SFR densities of Ouchi et al. (2004) at $z = 4$ –5 using their measured color excesses are actually marginally higher than we derive with the “common” obscuration correction.

2.3. UV Data at High z

At $z \gtrsim 2$, some clarification is necessary regarding the UV derived $\dot{\rho}_*$ measurements. The two UV measurements at $z \approx 2$ and 3 are taken from the Hubble Deep Field (HDF) sample of Arnouts et al. (2005) and have been corrected for obscuration by adding to them a constant FIR SFR density equal to that at $z = 1$ from Le Floc’h et al. (2005). The three UV points at $2 \lesssim z \lesssim 5$ with comparatively low $\dot{\rho}_*$ come from Bouwens et al. (2003a) and are based on photometric dropouts using the cloning technique detailed by those authors. These points are low, as they correspond to only the high- L end of the luminosity function, and are not used here in any subsequent analysis. The two UV measurements at $z \approx 4$ and 5 are from Ouchi et al. (2004), corrected using a “common” obscuration correction, and are marginally lower than the $\dot{\rho}_*$ derived by those authors using their measured $E(B - V)$ color excesses. This slight difference has a negligible impact on the fitted parametric forms detailed

below and does not affect any subsequent analysis. At $z \approx 6$, there are now a large number of estimates in the literature, primarily using the photometric dropout technique and hence relying on accurate photometry and color measurements, all of which are based on small, deep fields (including the HDF, the Great Observatories Origins Deep Survey [GOODS], and the UDF). The two highest measurements of $\dot{\rho}_*$ at $z \approx 6$ come from GOODS (Giavalisco et al. 2004) and i dropouts in two deep ACS fields (Bouwens et al. 2003b). These estimates appear to be high compared to subsequent photometric dropout analyses, and this seems to be a result of sample contamination due to large color uncertainties from low-S/N photometric measurements (A. Bunker 2005, private communication). These two points are not used in subsequent analysis. The lowest measurement of $\dot{\rho}_*$ at $z \approx 6$ is from Bunker et al. (2004), based on UDF dropouts, and probes to $0.1 L^*$. Contributions from fainter sources are unlikely to increase this measurement by more than a factor of 2. The measurement of $\dot{\rho}_*$ between these extremes comes from Bouwens et al. (2006), incorporating the largest current sample of i dropouts from the UDF, UDF parallels, and GOODS. This measurement supersedes an earlier measurement (Bouwens et al. 2004a) using only the UDF parallel fields, which is not shown.

Although the issue of dust obscuration at high redshift is still highly uncertain, some data are beginning to be obtained. In addition to the $E(B - V)$ estimates from Ouchi et al. (2004), intriguing evidence for significant obscuration ($A_V \approx 1$ mag) at $z = 6.56$ has recently been established through *Spitzer* observations of a lensed $\text{Ly}\alpha$ emitting source (Chary et al. 2005). This implies that the first epoch of star formation in this source must have occurred around $z \approx 20$, and moreover that the “common” obscuration corrections applied to UV–luminosity-based SFR densities at $3 \lesssim z \lesssim 6$ may not be unreasonable. This is also supported by spectroscopic $\text{Ly}\alpha$ emission measurements of Lyman break galaxies (LBGs) at $z \approx 5$ (Ando et al. 2005b), suggesting that the bright LBGs (at least) lie in dusty, chemically evolved systems at this redshift.

At redshifts $6 < z < 10$, there have also been recent exciting estimates of the SFH (Bouwens et al. 2004b, 2005b; Bouwens & Illingworth 2005a) based on UV luminosities inferred using the photometric dropout technique. These measurements strongly suggest that the decline in the SFH seen around $z \approx 6$ continues to higher redshifts. Given the very small samples involved, the complete uncertainty regarding the level of obscuration at these redshifts, and more importantly the minimal impact that these data have on the integrated properties of the SFH being explored here, we do not include these points in any of our subsequent analysis. It is interesting to note, however, that they do appear in general to be consistent with all our results based on the SFH at $z \lesssim 6$.

To summarize the impact of dust-obscuration corrections on the normalization of the SFH, first the corrections can obviously act only to increase, not decrease, the normalization. The technique of UV+FIR measurements gives an effective obscuration correction to the UV data, increasing from a factor of 2 at $z \approx 0$ up to a factor of 5 at $z \gtrsim 1$. These results are consistent with obscuration-corrected $\text{H}\alpha$ estimates for $\dot{\rho}_*$ spanning $0 < z \lesssim 2$ (the range for which $\text{H}\alpha$ estimates are available), suggesting that the extent of the obscuration correction is unlikely to be much smaller. For $0.5 \lesssim z \lesssim 2.5$, this becomes less of a concern, as the SFH is dominated by contributions from FIR measurements, unaffected by obscuration, which serve as a lower limit to the SFH normalization. At higher redshifts still, the issue is less clear, but the recent results indicated above suggest that, even up to $z \approx 6$, dust obscuration may be significant. For the

following analysis, the $\bar{\nu}_e$ flux is dominated by the $z \lesssim 1$ regime, where the obscuration correction seems fairly well constrained through the UV+FIR technique.

2.4. IMF Assumptions

While uncertainties in SFR calibration act to increase the scatter in the SFH, and uncertainties in dust obscuration can raise it to greater or lesser degrees, the choice of IMF is the only assumption that can systematically *decrease* the SFH normalization. While most authors over the past decade have assumed the traditional Salpeter (1955) IMF for convenience, observations within recent years have strongly ruled it out as a robust model for a universal IMF. A modified Salpeter form with a turnover below $1 M_\odot$, however, is still a reasonable model (e.g., Baldry & Glazebrook 2003), and other currently favored IMFs include those of Kroupa (2001), Baldry & Glazebrook (2003), and Weidner & Kroupa (2005, 2006).

The SFR calibrations for all indicators used here for deriving the SFH estimates (which are the same as in Hopkins 2004) are defined assuming the Salpeter (1955) IMF. The compilation of data by Hopkins (2004) converts SFH estimates from the literature to these calibrations, where necessary, to ensure consistent assumptions throughout. To convert SFH estimates to an alternative IMF assumption corresponds to a simple scale factor. This scale factor is typically established through population-synthesis modeling using codes such as PEGASE (Fioc & Rocca-Volmerange 1997), GALAXEV (Bruzual & Charlot 2003), or Starburst99 (Leitherer et al. 1999). These codes, given an input IMF and SFR, can be used to infer the luminosity at SFR-sensitive wavelengths (typically UV and $H\alpha$). For different IMFs, the ratio between the resulting luminosities for a fixed SFR is the required scale factor. To explore these scale factors, we used PEGASE.2 to infer the UV (2000 Å) and $H\alpha$ luminosities, given as input a fixed, constant SFR, for those IMFs not excluded by Baldry & Glazebrook (2003). We use the default PEGASE.2 values for most input parameters, including a close binary mass fraction of 0.05, evolutionary tracks with stellar winds, and the SN II model B of Woosley & Weaver (1995), but we specify an initial metallicity of $Z = 0.02$, evolving self-consistently. We refer the reader to Bruzual & Charlot (2003) for a comparison between GALAXEV and PEGASE.2 (see also Fardal et al. 2006, who explore the effect of different input metallicities). For IMFs with progressively shallower slopes, it can be seen that the $H\alpha$ and UV luminosities scale differently from those derived assuming the Salpeter (1955) IMF, with $H\alpha$ being enhanced more quickly than the UV. We choose to follow earlier work and rely on the UV luminosity for our IMF scale factors (e.g., Cole et al. 2001; Madau et al. 1998), but note that our results would change only marginally if we used the scale factors from the $H\alpha$ luminosities.

The scale factors derived for shallower (flatter or more top-heavy) IMFs are, in general, smaller than those for steeper IMFs. This results from the top-heavy IMFs producing more high-mass stars, and consequently more UV or $H\alpha$ luminosity, for a fixed total mass or SFR. Conversely, for a fixed UV or $H\alpha$ luminosity, a top-heavy IMF requires a lower SFR to reproduce that luminosity. We emphasize that here the *observed* quantity is the UV or $H\alpha$ luminosity, and the *derived* quantity is the SFR. We investigate here two extreme, but still realistic, IMF possibilities. The factor used to convert SFH measurements from a traditional Salpeter (1955) IMF (with a power-law slope of -1.35) to the IMF of Baldry & Glazebrook (2003), hereafter BG IMF, having a high-mass power-law slope of -1.15 , is 0.50 (-0.305 dex).

Note that Baldry & Glazebrook (2003) quote a high-mass slope of -1.2 in their Table 2 from the local $H\alpha$ luminosity density but also quote -1.15 as the best fit from the cosmic SFH. Here, as we are interested in the extremes, we choose to use the latter. If we used the scaling from the PEGASE.2 $H\alpha$ luminosity, we would have a factor of 0.41 rather than 0.50 for the BG IMF. All other IMFs explored here vary much less in the relative scaling for the $H\alpha$ and UV luminosities. To convert to the modified Salpeter A IMF (hereafter SalA IMF [Baldry & Glazebrook 2003], with high-mass power-law slope of -1.35) requires a factor of 0.77 (-0.114 dex). The Kroupa (2001) IMF (high-mass power-law slope of -1.3) and the modified Salpeter B IMF (hereafter SalB IMF [Baldry & Glazebrook 2003], high-mass power-law slope of -1.35) have scale factors intermediate between these choices. By exploring the impact of assuming the two extreme IMF choices, we expect to provide bounds encompassing the results of choosing any reasonable IMF in our subsequent analysis. We refer the reader to Figure 1 of Baldry & Glazebrook (2003) for an illustration of these and other IMFs from the literature, and also to Table 1 of Fardal et al. (2006).

The application of an IMF in this manner neglects, of course, the possibility that the IMF is not universal and indeed even likely to be evolving itself (e.g., Kroupa 2001). Different assumed star formation histories for our own galaxy may also affect estimates for the local IMF (see discussion by Elmegreen & Scalo 2006). At any epoch, however, the universe has some average IMF, which may have a large scatter around it for individual objects, and this average may vary with epoch. It is this average IMF that the SFH is sensitive to, and this may be different from what is inferred locally in the Milky Way. The current measurements do not yet support any detailed exploration of these issues, and we ignore them for the current analysis.

3. SFH FITTING

In order to derive a $\bar{\nu}_e$ flux from the DSNB for comparison with the limits from SK, it is necessary to fit some functional form to the SFH in order to facilitate integration over redshift. We choose to use the parametric form of Cole et al. (2001) that is now commonly used by many authors: $\dot{\rho}_* = (a + bz)h/[1 + (z/c)^d]$, where $h = 0.7$. The individual $\dot{\rho}_*$ measurements chosen to constrain this fit are also important, since the resulting fit will obviously vary depending on the data used. For $z \leq 1$, the SFH now appears to be very tightly constrained by the combination of UV data from SDSS (Baldry et al. 2005), COMBO17 (Wolf et al. 2003), and *GALEX* (Arnouts et al. 2005), corrected for obscuration using the *Spitzer* FIR measurements of Le Floc'h et al. (2005). This use of the FIR measurements of Le Floc'h et al. (2005) is further supported by their high level of consistency with those from Pérez-González et al. (2005) and the robust local 1.4 GHz estimate from Mauch (2005). As a consequence, we use only this set of corrected UV+FIR measurements, along with the $z = 0.01$ $H\alpha$ estimate of Hanish et al. (2006), to constrain the parametric fit for $z < 1$. For $z > 1$, we use all the data available in the compilation, with exceptions as noted above (the Thompson et al. 2006 UDF estimates, the two highest estimates at $z \approx 6$, and the three high- L -only estimates from Bouwens et al. 2003a), and we further exclude the six lowest measurements between $1 < z < 2$. The latter include the three highest redshift [O II] estimates from Hogg et al. (1998) and three UV estimates, where the “common” obscuration correction assumed is likely to significantly underestimate the true level of obscuration (compare the UV points between Figs. 1 and 2 of Hopkins 2004, for example). This is not unexpected, as the UV luminosity density, in

particular, at this redshift probes a very small fraction of the total $\dot{\rho}_*$ (see also Takeuchi et al. 2005).

The parametric fitting is a simple χ^2 fit to the 58 selected $\dot{\rho}_*$ measurements spanning $0 \leq z \leq 6$. The corresponding DSNB is calculated following the description in Beacom & Strigari (2006), their equations (1) and (2). The $\dot{\rho}_*(z)$ is first converted to a SN II rate history, $\dot{\rho}_{\text{SN II}}(z)$, scaling by the appropriate integral over the IMF

$$\dot{\rho}_{\text{SN II}}(z) = \dot{\rho}_*(z) \frac{\int_{8}^{50} \psi(M) dM}{\int_{0.1}^{100} M \psi(M) dM} \quad (1)$$

(see, e.g., Dahlen et al. 2004; Madau et al. 1998), where we have neglected the small delays due to the short lifetimes of SN II progenitors. For the two IMFs explored here, we have $\dot{\rho}_{\text{SN II}}(z) = (0.0132/M_\odot) \dot{\rho}_*(z)$ for the BG IMF and $\dot{\rho}_{\text{SN II}}(z) = (0.00915/M_\odot) \dot{\rho}_*(z)$ for the SalA IMF. This illustrates that the choice of IMF will affect the derived neutrino production through two separate but related normalizations. The first comes from how the IMF affects the normalization of the derived SFH from the observed UV, H α , or other SFR-sensitive luminosity, the second through this conversion of the SFH into a SN II rate history. The combination of these two factors to some degree converge on similar results, with steeper IMFs having higher SFH normalizations, but lower SN II rate scalings, and vice versa. As we show below, the BG IMF produces SN II rates that are a factor of $0.94 = (0.50/0.77) \times (0.0132/0.00915)$ of those from the SalA IMF (see also additional discussion below in § 5.2). We emphasize that, for a fixed UV, H α , or other SFR-sensitive luminosity, a shallower high-mass IMF produces fewer SNe II, while a steeper IMF produces more. If there are fewer SNe II, this will respect the upper limit on the DSNB flux but may start to conflict with direct measurements of $\dot{\rho}_{\text{SN II}}$ (which we take to be a lower limit) if too few SNe II are predicted. The converse applies for the steeper IMFs, with more SNe II predicted.

It should be noted, too, that the SN II rate could be derived more directly from, for example, the UV luminosity, rather than through the calibration to an SFR (representative of the whole mass range of an IMF), and then back to a SN II rate in this way. We use this method, as it conveniently allows the confidence-region fit to the SFH data to be used directly, rather than calculating different SN II rate conversions for each SFH measurement, depending on the SFR-sensitive wavelength. We have assumed throughout that all IMFs span the mass range $0.1 < M < 100 M_\odot$. Allowing a mass range up to $125 M_\odot$ alters most quantities by less than 1% and all quantities by less than 2%, significantly less than the variation between different IMF choices, the measurement uncertainties, or other uncertainties affecting the SFH normalization. The choice of stellar mass range that gives rise to SNe II is the largest assumption in this step. Restricting the upper mass limit to $30 M_\odot$ reduces the scale factor by about 10% in both cases. A much greater change is introduced by raising the lower mass limit. With a mass range of only $10 < M < 30 M_\odot$ in the numerator of equation (1), the resulting scale factors are reduced by $\approx 40\%$.

The predicted differential neutrino flux (per unit energy) is then calculated by integrating $\dot{\rho}_{\text{SN II}}(z)$ multiplied by the $\bar{\nu}_e$ emission per supernova, dN/dE' , appropriately redshifted, over cosmic time (Fukugita & Kawasaki 2003; Ando & Sato 2004; Strigari et al. 2004, 2005; Daigne et al. 2005; Lunardini 2005):

$$\frac{d\phi(E)}{dE} = c \int_{z=0}^6 \dot{\rho}_{\text{SN II}}(z) \frac{dN[E(1+z)]}{dE'} (1+z) \frac{dt}{dz} dz, \quad (2)$$

where $dt/dz = \{H_0(1+z)[\Omega_M(1+z)^3 + \Omega_\Lambda]\}^{-1/2}$, c is the speed of light, and we are evaluating the thermal emission spectrum

$$\frac{dN}{dE'}(E') = \frac{E_\nu^{\text{tot}}}{6} \frac{120}{7\pi^4} \frac{E'^2}{T^4} (e^{E'/T} + 1)^{-1} \quad (3)$$

at the appropriately redshifted energy $E' = E(1+z)$ (note the choice of units where $k = 1$, so that T has units of energy). Finally, $\int_{19.3 \text{ MeV}}^\infty (d\phi/dE) dE$ is calculated to establish the $\bar{\nu}_e$ flux for comparison with the SK limit of $1.2 \text{ cm}^{-2} \text{ s}^{-1}$ (Malek et al. 2003). The assumption of a thermal emission spectrum and the associated choices of temperature are determined by the eventual decoupling (after diffusion) of neutrinos from the hot and dense proto-neutron star, at a radius called the “neutrinosphere” (Raffelt 1996). We explore the implication of assuming a temperature of $T \approx 4, 6, \text{ or } 8 \text{ MeV}$ and, as in Beacom & Strigari (2006), we assume $E_\nu^{\text{tot}} = 3 \times 10^{46} \text{ J} = 3 \times 10^{53} \text{ ergs}$ for the total energy carried by all six neutrino flavors. While SNe emit all flavors of neutrinos and antineutrinos, and each is assumed to carry an approximately equal fraction of the total energy, at present the $\bar{\nu}_e$ flavor is the most detectable. Because the temperatures of the muon ($\bar{\nu}_\mu$) and tauon ($\bar{\nu}_\tau$) antineutrinos are expected to be higher than for $\bar{\nu}_e$, the effect of neutrino mixing may be to increase the observable $\bar{\nu}_e$ flux for a given SFH (Fukugita & Kawasaki 2003; Ando & Sato 2004; Strigari et al. 2004; Daigne et al. 2005); as in Beacom & Strigari (2006) and Yüksel et al. (2006), our results apply to an effective temperature after mixing, making them more constraining.

Given the $\bar{\nu}_e$ flux for each temperature, we simply scale the best-fitting SFH to ensure that the SK limit is not violated. This approach has the advantage that the shape of the SFH is determined only by measured data that is differential in redshift, while the normalization comes directly by imposing the SK $\bar{\nu}_e$ limit. We also explored an alternative approach that did not restrict the fitted shape of the SFH. In this approach, while iterating over the four fitting parameters, each new potential minimum χ^2 SFH is subjected to the DSNB limit, and the fit is rejected if the limit is violated. This technique resulted, for the higher $\bar{\nu}_e$ temperatures, in fitted SFHs that were significantly low (compared to the measurements) in the mid-to-high-redshift range, while still matching the $z = 0$ and $z \gtrsim 4$ SFH. For the low $\bar{\nu}_e$ temperatures, this method gave identical results to the original approach. Our preferred approach emphasizes the direct impact of the $\bar{\nu}_e$ data appropriately on the $z \lesssim 1$ measurements, as there are very few detectable neutrinos received from higher redshift. The best-fit SFHs independent of the $\bar{\nu}_e$ limit are identical to the fits constrained by a $\bar{\nu}_e$ temperature of $T = 4 \text{ MeV}$. As found and discussed in Yüksel et al. (2006), our results favor effective temperatures at the lower end of the predicted range (Keil et al. 2003; Thompson et al. 2003; Liebendoerfer et al. 2005; Sumiyoshi et al. 2005).

In addition to the Cole et al. (2001) parameterization, we also explored a piecewise linear SFH model in $\log(1+z) - \log(\dot{\rho}_*)$ space, in order to test the possibility that the Cole et al. (2001) parametric model could be biasing the shape of the resulting SFH fit in some way. In this model, we allow the following six parameters to vary: the $z = 0$ intercept, the slopes of three linear segments, and the two redshift values at which the slopes change. With this model, we similarly explore the range of $\bar{\nu}_e$ temperatures, as for the Cole et al. (2001) parameterization above.

4. RESULTS

Figure 1 shows the current SFH data compilation (assuming the SalA IMF) emphasizing the additional data used in this

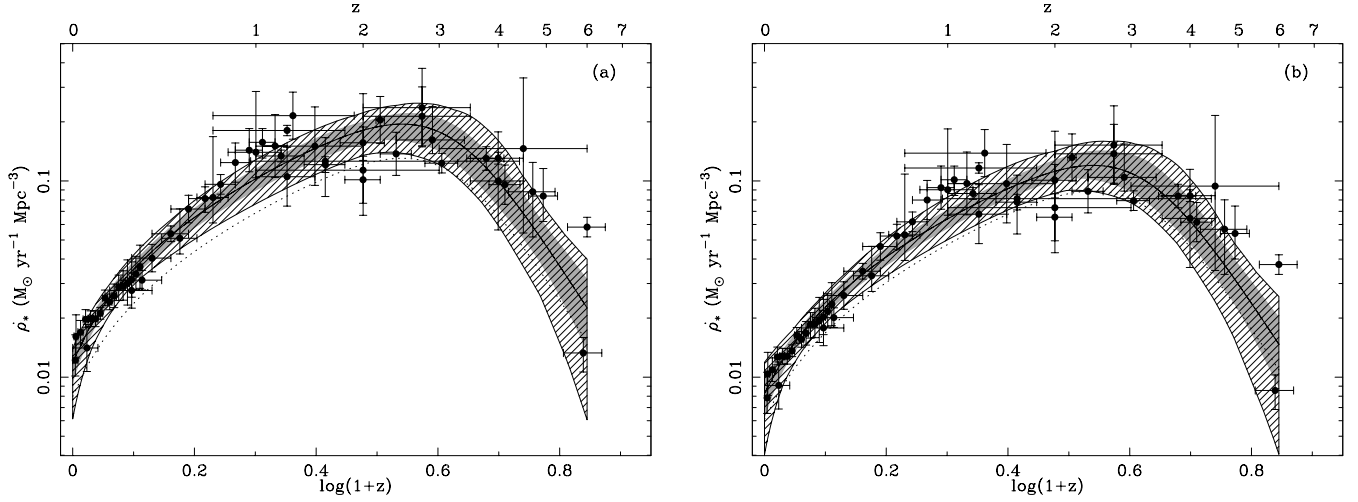


FIG. 2.— SFR density data used in defining the best-fitting parametric forms and the resulting fits, assuming (a) Salpeter IMF and (b) BG IMF. The shape of the fits is determined from the SFH data alone, and a scaling factor is fit to ensure consistency with the SK $\bar{\nu}_e$ limit (i.e., given the assumed temperature, this quantifies how much lower the SFH normalization has to be so as not to violate the SK limit). Solid lines assume a $\bar{\nu}_e$ temperature of $T = 4$ or 6 MeV, and dotted lines, $T = 8$ MeV. The gray shaded and hatched regions are, respectively, the 1 and 3σ confidence regions around the $T = 4$ MeV fits. The scaling factors are (a) 1.0 , 1.0 , and 0.67 and (b) 1.0 , 1.0 , and 0.74 , respectively, for $T = 4$, 6 , and 8 MeV.

analysis compared to the compilation of Hopkins (2004).⁵ The best-fitting Cole et al. (2001) form for this IMF is also shown ($a = 0.0170$, $b = 0.13$, $c = 3.3$, $d = 5.3$) as is the best-fitting piecewise linear fit. Figure 2 shows the data used in the fitting and the best fits, assuming three temperature values for the $\bar{\nu}_e$ population for each IMF assumed. The Cole et al. (2001) parameters for each case are given in Table 1. With 58 data points and 4 free parameters, there are 54 degrees of freedom, and the best-fitting χ^2 values (for the $T = 4$ MeV cases) are 37.5 for both the Salpeter IMF and the BG IMF. This value is perhaps somewhat lower than expected and reflects the nature of the uncertainties for the heterogeneous data used in the fit. These arise primarily from the Poisson counting statistics of the numbers of observed galaxies contributing to each measurement. No attempt has been made to resample or reanalyze independent data to appropriately combine their uncertainties, and the effect of multiple independent measurements at similar redshift, each with independently calculated uncertainties (since the data are heterogeneous), is to mimic conservative uncertainty estimates in a homogeneous data set. Correlations may also exist between assumed independent

SFH measurements at similar redshift, which may also contribute to the low χ^2 value. This may arise as a result, for example, of different teams independently analyzing the same data set or of independent analyses of common or overlapping survey areas, either at a range of wavelengths within the same survey or from surveys at different wavelengths of the same region of sky.

For both assumed IMFs, it can clearly be seen that the assumption of $T = 8$ MeV, when the SFH is required to be consistent with the $\bar{\nu}_e$ flux limit, is inconsistent with the SFH measurements. Also for both IMFs, the best-fitting SFH assuming $T = 6$ MeV is identical to that assuming $T = 4$ MeV. This can be understood by considering the Salpeter IMF, for example, with the higher SFH normalization, but which also has a lower conversion factor between $\dot{\rho}_*$ and $\dot{\rho}_{\text{SN II}}$, causing the predicted $\bar{\nu}_e$ flux to be within the SK limit, even with the assumption of the slightly higher neutrino temperature. For both IMF assumptions, we determine the 1σ (gray-shaded) and 3σ (hatched) confidence regions around the best-fitting SFH (corresponding to $T = 4$ or 6 MeV). These are derived from the regions of parameter space with $\chi^2 < \chi^2_{\text{min}} + \Delta\chi^2$, where $\Delta\chi^2 = 4.7$ and 16.0 , respectively, for 1 and 3σ (see Avni 1976, who shows that $\Delta\chi^2$ for q “interesting” parameters itself follows a χ^2 distribution with q degrees of freedom; here $q = 4$ for the Cole et al. 2001 parameterization). These confidence regions are determined independently at each redshift, intended to encompass the envelope of all fits. They are thus likely to be somewhat conservative, an effect that is compounded by the result of the χ^2 analysis being affected by what are effectively conservative measurement uncertainties. Subsequent figures reproduce these confidence regions in the predictions for stellar and metal mass density evolution [$\rho_*(z)$ and $\rho_Z(z)$, respectively] and SN rate evolution [$\dot{\rho}_{\text{SN}}(z)$]. The shapes of the $\bar{\nu}_e$ energy spectra corresponding to the various fits for the different IMF and temperature assumptions are shown in Figure 3. These results are very similar to the spectral shapes derived in Figure 1 of Beacom & Strigari (2006).

The results of the piecewise linear fitting, seen in Figure 4 and detailed in Table 2, are remarkably similar in general properties to the results in Figure 2. The gray shaded and hatched regions here again show, respectively, the 1 and 3σ confidence regions, here corresponding to $\Delta\chi^2 = 7.0$ and 19.8 (with $q = 6$). In this case, the perimeters of the confidence regions are not smooth, an artifact

⁵ The $\dot{\rho}_*$ data from Hogg et al. (1998) as given by Hopkins (2004) are incorrect, the result of an error in the cosmology conversion parameters used in that analysis. The correctly converted data are shown here and are smaller than those given by Hopkins (2004) by values decreasing monotonically from $\approx 43\%$ for the $z = 0.2$ bin to $\approx 30\%$ for the $z = 1.2$ bin. Sincere thanks go to Chun Ly for bringing this error to our attention.

TABLE 1
SFH PARAMETRIC FITTING TO THE FORM OF COLE ET AL. (2001)

Parameter	Modified Salpeter A IMF ^a	Baldry & Glazebrook (2003) ^b
a	0.0170	0.0118
b	0.13	0.08
c	3.3	3.3
d	5.3	5.2

^a For this fit, $\chi^2 = 37.5$. The scaling factors assuming $T = 4$, 6 , and 8 MeV are 1.0 , 1.0 , and 0.67 .

^b For this fit, $\chi^2 = 37.5$. The scaling factors assuming $T = 4$, 6 , and 8 MeV are 1.0 , 1.0 , and 0.74 .

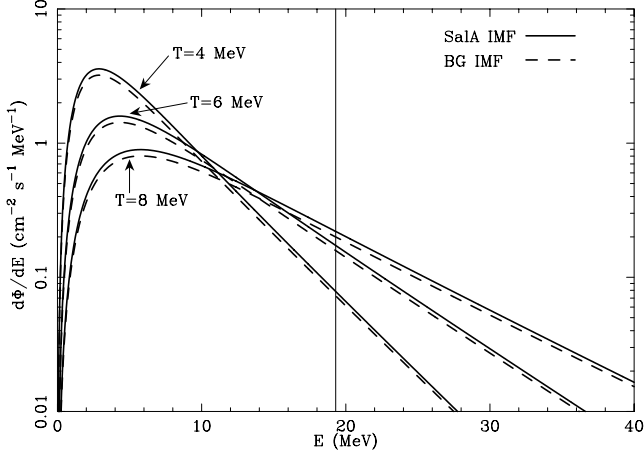


FIG. 3.—The $\bar{\nu}_e$ energy spectra predicted for the various SFH fits and temperature assumptions. The solid and dashed curves are the SalA IMF and BG IMF, respectively. The $T = 4$ and 6 MeV curves are consistent with the SK $\bar{\nu}_e$ limit. The $T = 8$ MeV curves are inconsistent with the $\bar{\nu}_e$ limit, and indicate the shape of the $\bar{\nu}_e$ spectrum derived by assuming the parametric form for the SFH corresponding to our best fit ($T = 4$ MeV) and setting the $\bar{\nu}_e$ temperature to the higher value. The thin vertical line marks $E = 19.3$ MeV, above which the $\bar{\nu}_e$ contributes to the SK limit.

arising from a combination of both the finite sampling of parameter space for which χ^2 values are calculated and the linear nature of the parameterization. With sufficiently high-resolution sampling of parameter space, the confidence region perimeters would be expected to curve more smoothly around the upper left and right corners. This artifact does not impact on any of our analyses, and as the confidence regions are mainly shown to illustrate the range of uncertainty in the fits, we do not pursue this issue further. The piecewise linear fits again show low values of χ^2 (see Table 2) for the same reasons as given above. The same preference for lower $\bar{\nu}_e$ temperatures is seen. The similarities here with the Cole et al. (2001) parameterization are encouraging and suggest that the Cole et al. (2001) parameterization has not introduced any significant bias against specific SFH shapes. For subsequent analysis, we retain the $T = 4$ MeV fits using the Cole et al. (2001) parameterization. This does not affect our conclusions, which remain unchanged regardless of which SFH parameterization we choose.

TABLE 2
PIECEWISE LINEAR SFH PARAMETRIC FITTING

Parameter ^a	Modified Salpeter A IMF ^b	Baldry & Glazebrook (2003) ^c
a	−1.82	−2.02
b	3.28	3.44
c	−0.724	−0.930
d	−0.26	−0.26
e	4.99	4.64
f	−8.0	−7.8
z_1	1.04	0.97
z_2	4.48	4.48

^a The parameters here are the intercepts and slopes of the linear segments in $\log(1+z) - \log(\dot{\rho}_*)$ space and the redshifts at which the slope changes. The parameters a and b are the intercept and slope for the line segment between $0 \leq z \leq z_1$; c and d are the intercept and slope between $z_1 \leq z \leq z_2$; e and f are the intercept and slope between $z_2 \leq z \leq 6$. All eight parameters are shown for convenience, but c and e are not independent and are not free parameters in the fitting.

^b For this fit, $\chi^2 = 19.8$. The scaling factors assuming $T = 4, 6$, and 8 MeV are $1.0, 1.0$, and 0.63 .

^c For this fit, $\chi^2 = 19.6$. The scaling factors assuming $T = 4, 6$, and 8 MeV are $1.0, 1.0$, and 0.67 .

Figure 5 shows the evolution of the stellar mass density, $\rho_*(z)$, along with the predictions from the best-fitting SFH for the two extreme IMF assumptions (compare with the extensive compilation of data in Fig. 4 of Fardal et al. 2006). To construct this diagram, we need to know the fraction of the stellar mass recycled into the interstellar medium as stellar winds or SN ejecta, R , corresponding to each IMF (Cole et al. 2001; Madau et al. 1998; Kennicutt et al. 1994). We follow the prescription suggested by Cole et al. (2001), using the models of Renzini & Voli (1981) and Woosley & Weaver (1995) for mass loss due to stellar winds and SNe, respectively, and calculate $R = 0.40$ for the SalA IMF and $R = 0.56$ for the BG IMF. The stellar mass inferred is then a fraction $(1 - R)$ of the time integral of the SFH (Cole et al. 2001). Converting the observed stellar mass density measurements (where a Salpeter IMF is most commonly used) to our assumed IMFs is achieved by scaling by the product of the SFR conversion factor and the ratio of the $1 - R$ factor for the chosen IMF to that of the Salpeter IMF (where $1 - R = 0.72$). The reliability of this method was confirmed by reproducing the stellar mass estimate, assuming the Kennicutt (1983) IMF by

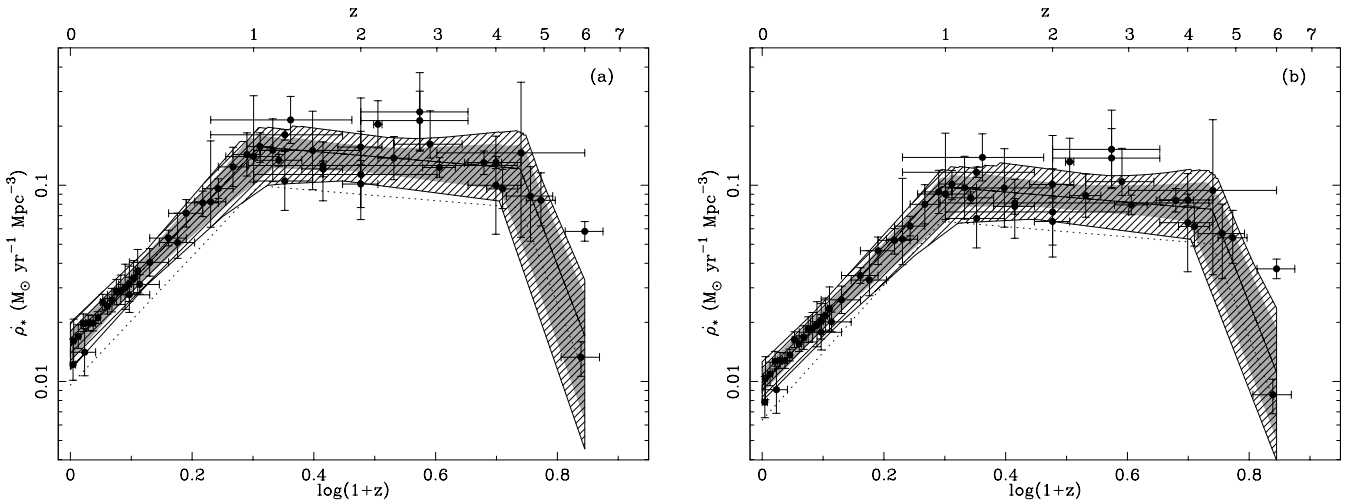


FIG. 4.—Same as Fig. 2, but assuming a piecewise linear SFH model, assuming (a) SalA IMF and (b) BG IMF. As before, solid lines assume a $\bar{\nu}_e$ temperature of $T = 4$ or 6 MeV, and dotted lines, $T = 8$ MeV.

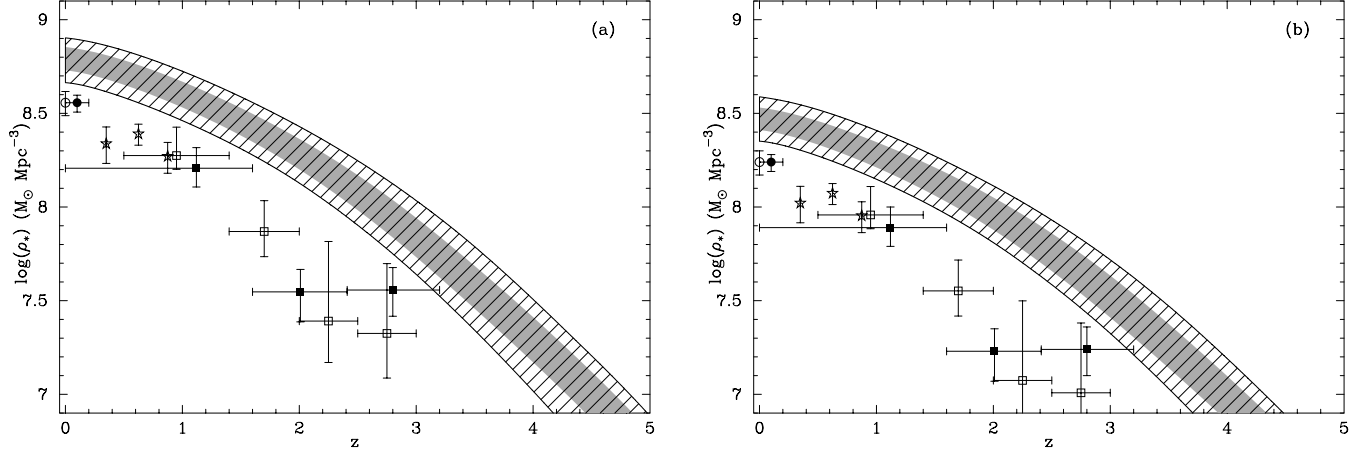


FIG. 5.— Evolution of stellar mass density buildup inferred from the SFH, assuming (a) Salpeter IMF (with $R = 0.40$) and (b) BG IMF (with $R = 0.56$). The gray shaded and hatched regions come from, respectively, the 1 and 3 σ confidence regions around the SFH $T = 4$ MeV fits. The details of scaling the data points to our assumed IMFs are given in the text. The open circle is the local stellar density from Cole et al. (2001); the filled circle and filled squares represent the SDSS and FIRES data, respectively, from Rudnick et al. (2003), scaled such that the SDSS measurement is consistent with that from Cole et al. (2001); the open stars are from Brinchmann & Ellis (2000), and the open squares are from Dickinson et al. (2003).

Cole et al. (2001), compared to their Salpeter IMF value. As a point of reference, using the Salpeter (1955) IMF where these scalings are not required, a diagram very similar to the current figure is shown in Figure 3 of Hopkins et al. (2005).

Both plots in Figure 5 show the measurements lying systematically below the predictions from the SFH, although the difference becomes more significant at higher redshift ($z \gtrsim 1.5$). Causes for the apparent inconsistency at high redshift have been discussed by other authors (e.g., Nagamine et al. 2004; Hopkins et al. 2005), who suggest that, in this regime, the observations might be missing up to half the stellar mass density. We discuss this, and the low-redshift discrepancy, further in § 5.

Figure 6 shows how the metal mass density evolves, $\rho_Z(z)$, as inferred from the SFH (Pei & Fall 1995; Madau et al. 1996; compare with Hopkins et al. 2005, and for a more detailed treatment of the evolution of separate metals, see Daigne et al. 2004). To determine this relation from the SFH, we assume that $\dot{\rho}_* = 63.7\dot{\rho}_Z$ (e.g., Conti et al. 2003). At $z = 0$, the compilation of data from Calura & Matteucci (2004) is shown, and these authors favor a value of $1.31 \times 10^7 M_\odot \text{Mpc}^{-3}$, toward the low end of the range. Values at $z = 0$ and 2.5 from Dunne et al. (2003) are also shown,

suggesting that the evolution in ρ_Z from the SFH may be consistent with that estimated from the dusty submillimeter galaxy (SMG) population, although recent results from Bouché et al. (2005) indicate that the SMGs may contribute much less to the metal mass density at high redshift.

Figure 7 shows the evolution in the SN rate for both SN Types Ia and II. Although the data to date are not yet precise, the SN rate data have a significant advantage over the stellar and metal mass density in that they are differential in redshift and are, in principle, more straightforward to measure. The SN II rate density, $\dot{\rho}_{\text{SN II}}$, is calculated from the SFH as described in equation (1). The SN Ia rate density, $\dot{\rho}_{\text{SN Ia}}$, is similarly estimated, although it involves more assumptions about the properties of SN Ia events than in the case of SNe II. In particular, the delay time t_{Ia} between star formation and the SN Ia event and the efficiency η of producing a SN Ia event from objects in the stellar mass range $3 < M < 8 M_\odot$ is not well constrained (and even this mass range is somewhat uncertain). Current estimates put t_{Ia} roughly in the range of 1–3 Gyr and η of the order of 1%–5% (see discussion in Strigari et al. 2005, and references therein). We follow Strigari et al. (2005) in assuming

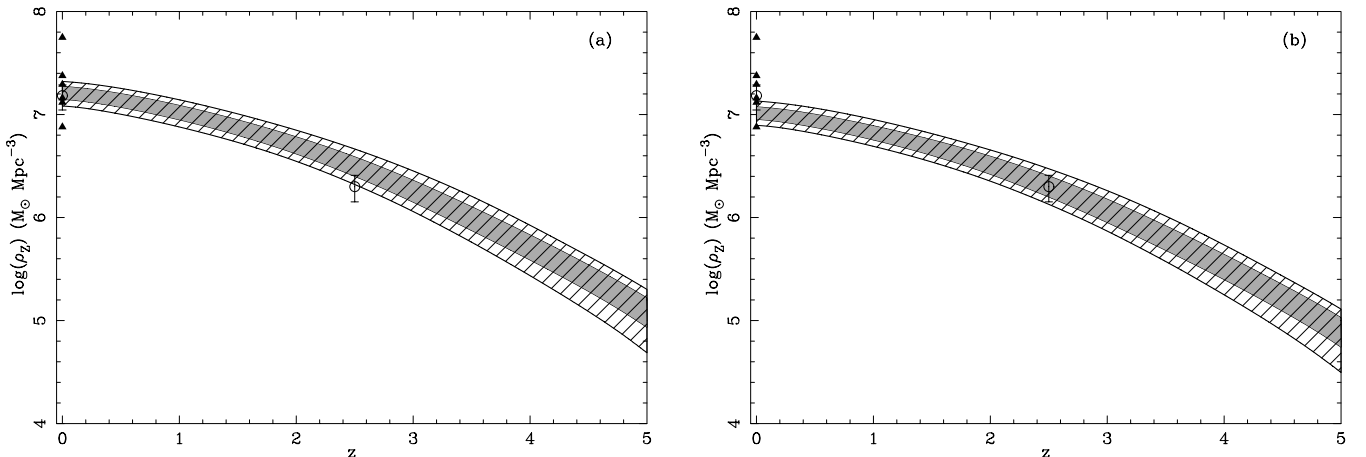


FIG. 6.— Evolution of metal mass density buildup inferred from the SFH, assuming (a) Salpeter IMF and (b) BG IMF. The gray shaded and hatched regions come from the 1 and 3 σ confidence regions around the SFH $T = 4$ MeV fits respectively. The triangles at $z = 0$ are from Calura & Matteucci (2004), and the open circles at $z = 0$ and ≈ 2.5 are from Dunne et al. (2003).

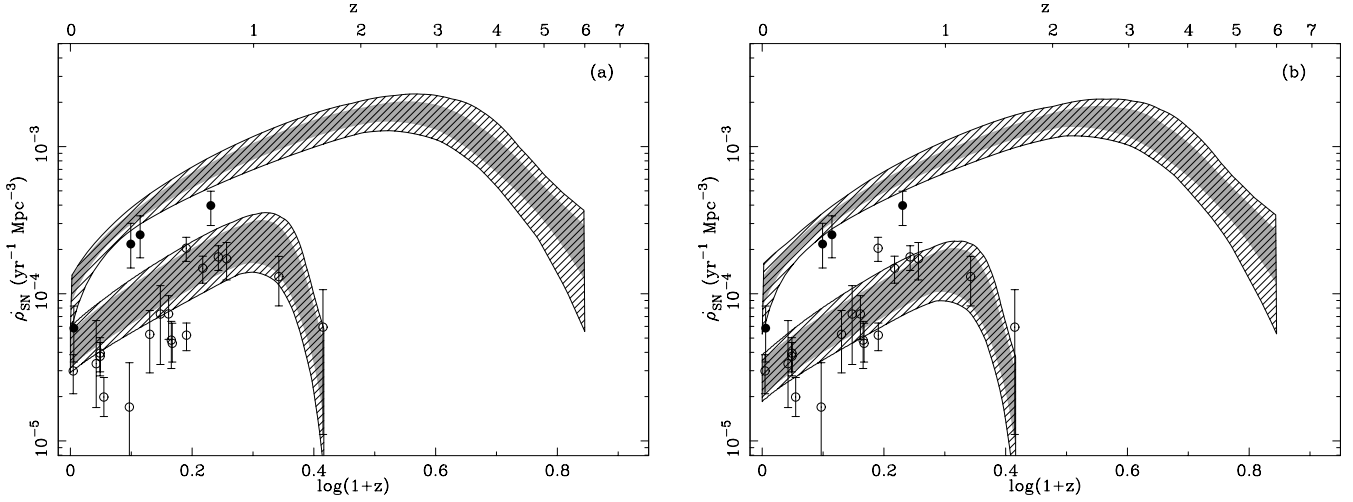


FIG. 7.—Evolution of SN rates inferred from the SFH. The upper curves correspond to the predictions for $\dot{\rho}_{\text{SN II}}$, and the lower, for $\dot{\rho}_{\text{SN Ia}}$, assuming a delay time $t_{\text{Ia}} = 3$ Gyr. Panel (a) assumes SalA IMF, and (b) assumes BG IMF. The gray shaded and hatched regions again come from the 1 and 3 σ confidence regions around the SFH $T = 4$ MeV fits respectively, except that for the SN Ia region, the lower bound comes from assuming $f_{\text{Ia}} = 1/1000 M^{-1}_{\odot}$, while the upper bound assumes $f_{\text{Ia}} = 1/700 M^{-1}_{\odot}$. The filled circles are $\dot{\rho}_{\text{SN II}}$ measurements from Dahlen et al. (2004) and Cappellaro et al. (2005). The open circles are $\dot{\rho}_{\text{SN Ia}}$ measurements reproduced from the compilation of Strolger & Reiss (2006) and the data of Barris & Tonry (2006) and Neill et al. (2006).

a constant $t_{\text{Ia}} = 3$ Gyr and $f_{\text{Ia}} = 1/700 M^{-1}_{\odot}$, where $f_{\text{Ia}} = \eta \int_3^8 \psi(M) dM / \int_{0.1}^{100} M \psi(M) dM$, to determine $\dot{\rho}_{\text{SN Ia}}$ from

$$\dot{\rho}_{\text{SN Ia}}(t) = \eta \frac{\int_3^8 \psi(M) dM}{\int_{0.1}^{100} M \psi(M) dM} \dot{\rho}_*(t - t_{\text{Ia}}). \quad (4)$$

For the SalA and BG IMFs, $f_{\text{Ia}} = 0.028\eta$ and $f_{\text{Ia}} = 0.032\eta$, respectively. With our assumed value of f_{Ia} , this corresponds to assuming $\eta \approx 5\%$ for both IMFs. Figure 7 also shows the effect of assuming $f_{\text{Ia}} = 1/1000 M^{-1}_{\odot}$ in the lower limit of the 1 and 3 σ envelopes for the predicted $\dot{\rho}_{\text{SN Ia}}$. Figure 8a reproduces Figure 7b with the assumption of $t_{\text{Ia}} = 1$ Gyr, illustrating the effect of the different delay times. This produces a somewhat reduced $\dot{\rho}_{\text{SN Ia}}$ envelope at lower redshifts and moves the turnover to higher redshifts.

5. DISCUSSION

5.1. Stellar Mass and Metal Mass Densities

The predictions from the SFH for both $\rho_*(z)$ and $\rho_Z(z)$ are difficult to analyze, for different reasons. Most predictions of

$\rho_*(z)$ based on SFH measurements seem to be larger than the observed stellar mass density at high redshift, and numerous simulations imply that the measurements might be underestimating the total $\rho_*(z)$ (e.g., Nagamine et al. 2004; Menci et al. 2004; Somerville et al. 2001; Granato et al. 2000). Indeed, it is suggested by Dickinson et al. (2003) that additional obscuration added to their maximally old component used in estimating stellar masses could cause arbitrarily large masses to be derived, and it is perhaps not unreasonable to expect stellar mass densities a factor of ~ 2 larger as a result of reasonable obscuration levels. This would bring the measurements more into line with the predictions from the SFH. Similar issues may affect the other high-redshift measurements of $\rho_*(z)$; other issues that have been raised include incomplete galaxy population sampling and cosmic variance, which may affect surveys probing small fields of view (see discussion in Nagamine et al. 2004).

At low redshift, the discrepancy between the measurements of $\rho_*(z)$ and the SFH prediction is more of a concern. A first attempt at resolving this might be to suggest that the measured SFH is too high at $z = 0$, and the technique used (combining $\dot{\rho}_*$

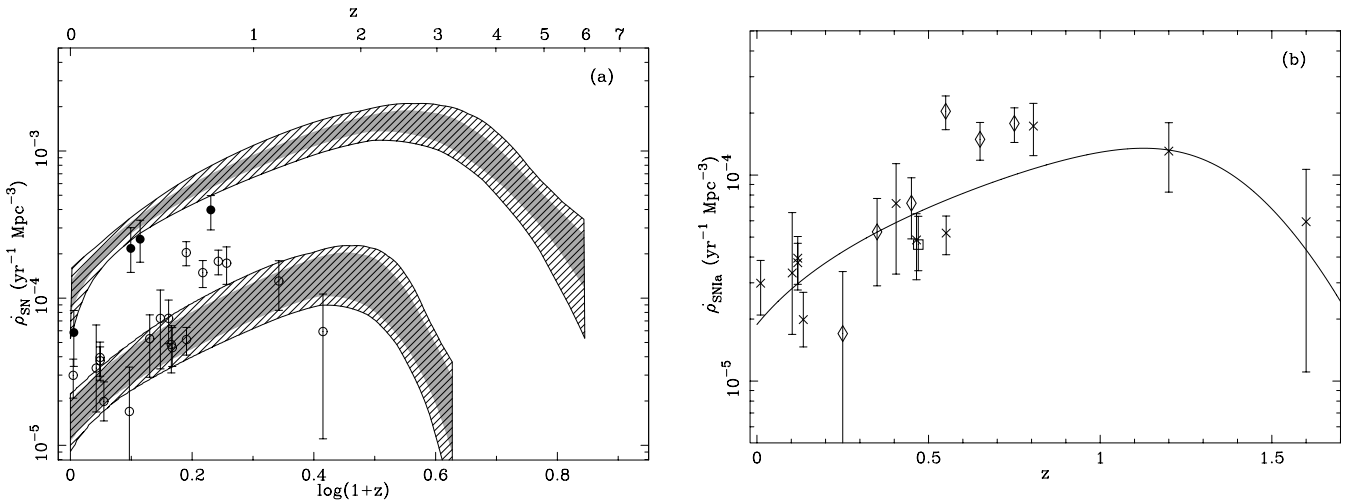


FIG. 8.—(a) Same as for Fig. 7b, but assuming $t_{\text{Ia}} = 1$ Gyr. (b) The best fit to the SN Ia rate from the SFH, with $A = 1.15 \times 10^{-3}$ and $t_{\text{Ia}} = 2.7$ Gyr (see text). Crosses are the data compilation from Strolger & Reiss (2006), diamonds are data from Barris & Tonry (2006), and the square is from Neill et al. (2006). Note different axes ranges from (a) and the linear redshift scale.

from FIR and UV estimates) is not accurate. This cannot be the whole solution, as it does not address the problem at $z \approx 1$, where the SFH is dominated by the FIR contribution, and the $\rho_*(z)$ values inferred from the SFH are similarly higher than the measurements. Another point against this solution is the equivalent diagram in Figure 3 of Hopkins et al. (2005), where (for a Salpeter IMF) a broader region, encompassing the majority of SFH measurements, is used to predict $\rho_*(z)$, rather than the confidence regions fitted here. Even in that diagram, the $\rho_*(z)$ measurement at $z = 0$ lies at the extreme lower boundary of the SFH prediction. This suggests that there is something more subtle underlying this discrepancy than simple obscuration-correction errors in the SFH. A partial solution might be found through the underlying measurement techniques used for the different quantities. The SFH measurements rely on inferring SFRs from the luminosity generated by massive stars, while the $\rho_*(z)$ measurements come by inferring total stellar masses based on the luminosity of low-mass stars. These are connected in the prediction of $\rho_*(z)$ from the SFH through the assumed IMF shape, and it is possible that the discrepancy seen in Figure 5 may be reflecting limitations in our understanding of the relative shapes of the low- and high-mass ends of our assumed IMFs. Although further exploration of this discrepancy is beyond the scope of the present investigation, we refer the reader to Fardal et al. (2006), who provide a detailed analysis of this issue, incorporating limits from the total extragalactic background radiation along with the SFH and stellar mass evolution.

Regarding the evolution of the metal mass density, $\rho_Z(z)$, the investigation of predictions from the SFH is complicated by the limited number of estimates for this quantity at $z > 0$. This is observationally a difficult measurement to make, particularly as much of the metals may exist in an ionized intergalactic medium component. Measurements of the contributions from various components (stellar, dust, and gas) have been explored, with varying estimates for how much of the metal mass density budget might be contained in different components at high redshift (e.g., Dunne et al. 2003; Bouché et al. 2005). Additional discussion of this issue, emphasizing the (minimal) contribution from damped Ly α absorbers, is presented by Hopkins et al. (2005).

5.2. Supernovae Type II

Almost identical predictions for $\dot{\rho}_{\text{SN II}}$ are obtained for both the SalA and SalB IMFs detailed in Baldry & Glazebrook (2003), a consequence of SalA having a slightly higher conversion factor than SalB for transforming $\dot{\rho}_*$ from the traditional Salpeter IMF, and a slightly lower conversion factor to transform between $\dot{\rho}_*$ and $\dot{\rho}_{\text{SN II}}$. The BG IMF result (Fig. 7b) appears to be marginally more consistent with both the $\dot{\rho}_{\text{SN II}}$ and $\dot{\rho}_{\text{SN Ia}}$ measurements than the prediction assuming the SalA IMF (Fig. 7a), although both are acceptable. The uncertainties affecting the $\dot{\rho}_{\text{SN II}}$ measurements are treated in some detail by Dahlen et al. (2004), and the error bars shown are representative of the combination of both statistical and systematic uncertainties. The $z = 0$ measurement may be somewhat low, and recent investigations (Mannucci et al. 2003; Ando et al. 2005a) suggest that this point is in fact likely to be higher by a factor of 2 or 3, consistent with the SFH predictions. Dahlen et al. (2004) indicate that the main concern in the measurements is the level of obscuration, and that a change from their assumed $E(B - V) = 0.15$ of $\Delta E(B - V) = \pm 0.06$ would alter their measurements by 1 standard deviation. It is certainly likely that this is the case for the highest redshift point at $z = 0.7$, where obscuration is expected to be higher than at lower redshifts (e.g., Takeuchi et al. 2005; Hopkins 2004; see also Fig. 1). This would have the

effect of raising the $z = 0.7$ measurement to be consistent with the predictions from the SFH.

The $\dot{\rho}_{\text{SN II}}$ measurements provide a strong lower bound on the normalization of the SFH. Particularly given that uncertainty regarding obscuration corrections is more likely to raise than lower the $\dot{\rho}_{\text{SN II}}$ measurements, the SFH normalization cannot realistically be much lower than that obtained from assuming the BG IMF (Fig. 2b). The scaling factors for the SFH fits suggest that this provides further evidence against the $T = 8$ MeV assumption for both assumed IMFs. Moreover, the $\dot{\rho}_{\text{SN II}}$ measurements are unlikely to be affected by sufficient obscuration to support an SFH normalization much higher than that obtained with the SalA IMF. The level of obscuration to be inferred in order to make the $\dot{\rho}_{\text{SN II}}$ measurements lie above the upper edge of the SalA IMF envelope requires $E(B - V) \approx 0.3$ at $z = 0.3$ and $E(B - V) \approx 0.5$ at $z = 0.7$. These values are quite extreme, corresponding to correction factors of approximately 3.3 and 6, respectively, and values this high are not even inferred from the luminosity-dependent obscuration corrections of Hopkins (2004) for UV data at similar redshifts. Higher SFH normalizations may still be possible, however, and here we return to the assumptions regarding the mass range over which we assume stars become core-collapse SNe. If we allow only a mass range of $10 < M < 30 M_\odot$, the $\dot{\rho}_{\text{SN II}}$ predictions from the SalA IMF would be lowered by as much as a factor of 0.6 (-0.2 dex). Assuming this mass range would place predictions from even the traditional Salpeter IMF at such a level (i.e., ≈ -0.2 dex from the confidence region in Fig. 7a). So, at the expense of an increased lower limit of integration for core-collapse SN production, IMFs providing quite high normalizations for the SFH can still be made consistent with the $\dot{\rho}_{\text{SN II}}$ measurements.

Another point to be considered here is the issue of a possible neutrino flux generated from a population of massive stellar objects not observable as SNe II (Beacom et al. 2001; Heger et al. 2003; Strigari et al. 2005; Daigne et al. 2005). For example, if stars in the mass range $30 < M < 50 M_\odot$ produce the same kind of burst of neutrinos at the end of their lives as SNe II, but do not become core-collapse SNe, instead progressing directly to a black hole or other exotic end, then the neutrino flux inferred from the SFH via an assumed SN II rate will be biased, and the observed SN II rate density could legitimately be $\approx 10\%$ lower than that predicted from the SFH using this technique. If even lower-mass progenitors become failed SNe, then this difference could be even larger. Certainly more robust information regarding the connection between the final stages of stellar evolution and neutrino emission would help to refine this type of analysis, and strengthen the implications regarding the favored SFH normalization and corresponding IMF.

Our general conclusions here are that (1) the IMF cannot be much more shallow at the high-mass end than the BG IMF without predicting values for $\dot{\rho}_{\text{SN II}}$ that are too low (see also Loewenstein 2006); and (2) in the absence of a lower integration limit as high as $\approx 10 M_\odot$ for core-collapse SN production, the IMF cannot produce SFH normalizations much higher than does the SalA IMF without predicting values for $\dot{\rho}_{\text{SN II}}$ that begin to require quite extreme obscuration corrections. Some slightly less extreme IMFs, while still producing higher SFH normalizations than the SalA IMF, may be allowed if the core-collapse SN lower mass cutoff lay between 8 and $10 M_\odot$. This would still seem to be hard to justify, however, as evidence is growing for SN progenitors at these low masses. The SN II analyzed by Van Dyk et al. (2006), for example (2003gd), favors a progenitor mass of 8–9 M_\odot (see also Smartt et al. 2004). A second SN II (2005cs) also favors a

low progenitor mass, $9_{-2}^{+3} M_{\odot}$ (Maund et al. 2005). To confirm and refine these IMF constraints, a larger selection of independent $\dot{\rho}_{\text{SN II}}$ measurements, spanning a broad range of redshift, would be invaluable. As noted in Strigari et al. (2005), sufficiently precise SN II rate data could be used to directly predict the DSNB flux, independently of assumptions about the SFH and IMF.

5.3. Supernovae Type Ia

The prediction for $\dot{\rho}_{\text{SN Ia}}$ from the SFH is also particularly intriguing. The assumption of the fixed $t_{\text{Ia}} = 3$ Gyr has the effect of matching the $z \gtrsim 3$ turnover in the fitted SFH with the apparent decline in $\dot{\rho}_{\text{SN Ia}}$ seen in the highest redshift measurement from the GOODS sample of Dahlen et al. (2004). It is possible, indeed probable, that this is simply a coincidence, as it is a single $\dot{\rho}_{\text{SN Ia}}$ measurement, with large uncertainties, that is suggestive of the decline, and the turnover in the SFH is driven almost entirely by the $z \approx 6$ measurement of Bunker et al. (2004). It is thus still highly possible that the decline in both the SFH and $\dot{\rho}_{\text{SN Ia}}$ lie at somewhat higher redshift. In particular, recent spectroscopic results from a complete magnitude-limited sample (Le Fèvre et al. 2005) suggest that the SFH inferred at $z = 3-4$ is up to 2 or 3 times higher than that estimated from color-selected LBGs (Steidel et al. 1999). This may imply that the shape of the SFH is flatter between $2 < z < 6$ than our current fits suggest. Even more tantalizingly, the higher SFH estimates from the spectroscopic measurements compared to the color-selected samples at $3 < z < 4$ suggest that the photometric-dropout-selected samples at even higher redshift ($z \approx 6$) may also be underestimating the total SFH. This effect would be compounded by the recent evidence suggesting nonnegligible obscuration at high z (Chary et al. 2005; Ando et al. 2005b), and appears to provide evidence that the expected high-redshift decline in the SFH may still not be well established. With this in mind, it is nonetheless interesting to note that the robustness of the GOODS measurements, again, has been explored in some detail by Dahlen et al. (2004), who are confident of the reliability of this feature in the $\dot{\rho}_{\text{SN Ia}}$ data. If the turnover in the SFH also turns out to be reliable, the $\dot{\rho}_{\text{SN Ia}}$ evolution can be used to constrain the delay time for SNe Ia (e.g., Förster et al. 2006). The predictions for $\dot{\rho}_{\text{SN Ia}}$ are quite different for $t_{\text{Ia}} = 1$ Gyr (Fig. 8a) compared with $t_{\text{Ia}} = 3$ Gyr, and refining the measurements of $\dot{\rho}_{\text{SN Ia}}$ between $1 < z < 3$ would be quite revealing. Alternatively, if the SFH turnover does indeed lie at $z > 6$, this would imply either that $t_{\text{Ia}} > 3$ Gyr, a result that appears to lie outside the currently favored range, or that the true turnover in the $\dot{\rho}_{\text{SN Ia}}$ measurements is also at somewhat higher redshift than the $z \approx 1.5$ from Dahlen et al. (2004).

To explore a more physically motivated connection between SN Ia generation and the underlying stellar populations, Scannapieco & Bildsten (2005) introduced a two-component model, dependent on both SFR and stellar mass densities, to derive the SN Ia rate density. This has the effect of allowing a contribution to the SN Ia rate from old stellar populations, where the current SFR may be low, while maintaining a contribution from the currently star-forming systems. Taking a logical next step, Neill et al. (2006) allow a delay time to be incorporated into such a two-component model, and find a characteristic delay time $\tau = 3$ Gyr (given a Gaussian distribution of delay times), consistent with our simple result above, although their model also includes a contribution from a component proportional to ρ_* . Mannucci et al. (2006) find a bimodal distribution of delay times, with a “prompt” component having a delay time of ≈ 0.1 Gyr (Pinsonneault & Stanek 2006 find evidence that the joint IMF of binary stars favors “twins” of nearly equal mass, and suggest that this may provide a natural explanation for these prompt SNe Ia).

To illustrate the power of a well-constrained SFH, we use our best-fitting SFH for the BG IMF (from Table 1) to explore the available parameters in a Scannapieco & Bildsten (2005) model and, keeping in mind the cautions regarding the high-redshift declines in both $\dot{\rho}_{\text{SN Ia}}$ and $\dot{\rho}_*$, do not try to overinterpret our results. We explored the connection between $\dot{\rho}_{\text{SN Ia}}$, $\dot{\rho}_*$ and ρ_* using the relation

$$\dot{\rho}_{\text{SN Ia}}(t) = A\dot{\rho}_*(t - t_{\text{Ia}}) + B\rho_*(t), \quad (5)$$

with all quantities in the physical units used in this investigation. Performing a simple χ^2 minimization, allowing A , B and t_{Ia} to vary, we find that the best-fitting solution favors $A = 1.15 \times 10^{-3} M_{\odot}^{-1}$, $B = 0 M_{\odot}^{-1} \text{ yr}^{-1}$, and $t_{\text{Ia}} = 2.7$ Gyr. This result is illustrated in Figure 8b, and is clearly driven fairly strongly (as expected intuitively from Fig. 7) by the combination of the high- z $\dot{\rho}_{\text{SN Ia}}$ measurement and the turnover in the SFH driven by the Bunker et al. (2004) measurement. The value of $A = 1.15 \times 10^{-3} M_{\odot}^{-1}$ is consistent with the range of $0.001 \leq f_{\text{Ia}} \leq 0.0014 M_{\odot}^{-1}$ assumed for the limits in Figure 7. The $B = 0$ result seems to arise from the strong similarity in shape between the SFH and the $\dot{\rho}_{\text{SN Ia}}(z)$ evolution, while the $\rho_*(z)$ evolution has the opposite shape (increasing to lower redshifts, rather than decreasing). It seems clear that allowing negative values of B would allow some nonzero solution, although what physical interpretation this would have is not clear. It certainly would not be in the spirit of the model as intended by Scannapieco & Bildsten (2005). As concluded above, and since $B = 0$, our tentative inference appears to favor SN Ia delay times close to $t_{\text{Ia}} \approx 3$ Gyr, although there are clearly much more sophisticated models, including those allowing for a distribution in delay times that we have not explored here, and the locations of the apparent downturns in both $\dot{\rho}_{\text{SN Ia}}$ and $\dot{\rho}_*$ clearly have a very strong influence on this result.

5.4. Detecting the DSNB

With the best-fitting SFH models explored here, the predictions for the DSNB appear to lie excitingly close to the measured $\bar{\nu}_e$ flux limit (Fig. 3). It is clear that directly observing the DSNB will allow much greater insight into the properties of star formation. Already the DSNB constraint indicates a preferred IMF range and normalization for the SFH. It also illustrates that stronger constraints on the SFH have implications for understanding the details of both SN II and SN Ia production, and the physical basis of neutrino generation by SN II is intimately associated with all these predictions. Being able to detect the DSNB and its energy spectrum will allow a more sophisticated analysis of the detailed connections between all these aspects of star formation and the cosmic SFH.

Methods for increasing the sensitivity of particle detectors to DSNB antineutrinos and neutrinos have been detailed elsewhere, and we briefly reiterate some of these conclusions, to illustrate the potential for detecting the DSNB. Beacom & Vagins (2004) propose loading SK with dissolved gadolinium trichloride (GdCl_3) to allow tagging of neutron captures, thus significantly lowering backgrounds, in order to directly detect the DSNB $\bar{\nu}_e$ spectrum. This provides perhaps the best immediate possibility for measuring the DSNB spectrum shape, which, given the minimum normalization of the SFH assuming the BG IMF, seems to be lying just below the current flux limit. Beacom & Strigari (2006) describe how the Sudbury Neutrino Observatory (SNO) could improve the current flux limit for DSNB ν_e by about 3 orders of magnitude by coupling the background analysis from SK with the sensitivity to ν_e at SNO. Combining information on both

DSNB ν_e and $\bar{\nu}_e$ populations will allow further exciting insight and constraints on SN II neutrino production (the connection between the two is explored further by Lunardini 2006).

6. SUMMARY

We have updated the SFH compilation of Hopkins (2004), emphasizing the strong constraints from recent UV and FIR measurements and refining the results of numerous measurements over the past decade. An analysis of various uncertainties that may contribute to the normalization of the SFH has been performed, and the IMF assumption plays a key role, being essentially the only assumption that can lower the normalization. We performed parametric fits to the SFH using the form of Cole et al. (2001) and piecewise linear models, both constrained by the SK $\bar{\nu}_e$ limit. The results suggest that the preferred IMF should produce SFH normalizations within the range of those from the modified Salpeter A IMF (Baldry & Glazebrook 2003) and the IMF of Baldry & Glazebrook (2003). They also suggest that lower temperatures ($T = 4\text{--}6$ MeV) are preferred for the $\bar{\nu}_e$ population. It should be noted that here we have assumed a simple Fermi-Dirac spectrum for the $\bar{\nu}_e$ spectrum after neutrino mixing. However, since the current SK energy threshold (19.3 MeV) is so high, the DSNB flux limit is sensitive to the assumed shape of the spectrum, and a reduction in the height of the spectral tail would allow a higher average neutrino energy. This highlights the importance of lowering the energy threshold (Beacom & Vagins 2004; Yüksel et al. 2006). In addition, a more accurate treatment of future data would be based not on the integrated flux above the energy threshold, but rather on the detected event rate spectrum above the energy threshold (Yüksel et al. 2006) after weighting with the neutrino interaction cross section (Vogel & Beacom 1999).

Based on the fits to the SFH, we predict the evolution of ρ_* , ρ_Z , and $\dot{\rho}_{\text{SN}}$ and compare with observations. The comparisons with $\dot{\rho}_{\text{SN}}$ are most revealing, providing the limitations on the assumed IMF and tentatively favoring longer delay times ($t_{\text{la}} = 3$ Gyr) for the SN Ia population. The $\dot{\rho}_{\text{SN II}}$ measurements provide a key constraint on the SFH normalization, and correspondingly on the favored IMF. In particular, these data bound the SFH from

below, while the DSNB bounds the SFH from above (due to the SK energy threshold, the DSNB flux limit primarily constrains SNe II with $z \lesssim 1$, the same range in which we wish to test the factors that normalize the SFH). Together, these provide a novel technique for testing or verifying measurements of a universal IMF and emphasize the importance of understanding the range of stellar masses leading to the various stellar evolution core-collapse outcomes. More measurements of $\dot{\rho}_{\text{SN}}$ for both SNe II and Ia over a broader redshift range (Oda & Totani 2005; Mesinger et al. 2006) would help to more strongly constrain both the preferred universal IMF and the properties of SNe. Observing the high-redshift turnover in the SN Ia rate would also have strong implications for the location of the expected high-redshift turnover in the SFH. Direct observation of the DSNB will clearly allow much greater insight into the physics and astrophysics of star formation and supernovae. Given the power of the existing SK $\bar{\nu}_e$ flux limit, any improvements in sensitivity will have a very strong impact on constraining the product of the dust corrections, IMF normalization, and neutrino emission per supernova. In fact, since reasonable choices for all of these already saturate the SK limit, we expect that the significantly improved sensitivity which would be enabled by adding gadolinium to SK (Beacom & Vagins 2004) should lead to a first detection of DSNB $\bar{\nu}_e$ (Beacom & Vagins 2004; Strigari et al. 2004, 2005; Daigne et al. 2005; Yüksel et al. 2006).

The authors would like to thank the referee, Shaun Cole, for rectifying a misconception in an early draft of this manuscript, and for helpful suggestions leading to the current and much improved version. We also thank Andy Bunker, Mark Fardal, Louie Strigari, and Mark Sullivan for helpful comments and interesting discussions, and Don Neill for providing a copy of Neill et al. (2006) prior to submission. A. M. H. acknowledges support provided by the Australian Research Council in the form of a QEII Fellowship (DP0557850). J. F. B. acknowledges support from Ohio State University and NSF CAREER grant PHY-0547102.

REFERENCES

- Afonso, J., Hopkins, A., Mobasher, B., & Almeida, C. 2003, *ApJ*, 597, 269
Ando, S. 2004, *ApJ*, 607, 20
Ando, S., Beacom, J. F., & Yüksel, H. 2005a, *Phys. Rev. Lett.*, 95, 171101
Ando, M., Ohta, K., Iwata, I., Akiyama, M., Aoki, K., & Tamura, N. 2005b, in *The Fabulous Destiny of Galaxies: Bridging Past and Present*, in press (astro-ph/0510830)
Ando, S., & Sato, K. 2004, *New J. Phys.*, 6, 170
Arnouts, S., et al. 2005, *ApJ*, 619, L43
Avni, Y. 1976, *ApJ*, 210, 642
Baldry, I. K., & Glazebrook, K. 2003, *ApJ*, 593, 258
Baldry, I. K., et al. 2005, *MNRAS*, 358, 441
Barris, B. J., & Tonry, J. L. 2006, *ApJ*, 637, 427
Beacom, J. F., Boyd, R. N., & Mezzacappa, A. 2001, *Phys. Rev. D*, 63, 073011
Beacom, J. F., & Strigari, L. E. 2006, *Phys. Rev. C*, 73, 035807
Beacom, J. F., & Vagins, M. R. 2004, *Phys. Rev. Lett.*, 93, 171101
Bell, E. 2003a, *ApJ*, 586, 794
———. 2003b, *RevMexAA*, 17, 163
Bell, E., et al. 2005, *ApJ*, 625, 23
Bouché, N., Lehnert, M. D., & Péroux, C. 2005, *MNRAS*, 364, 319
Bouwens, R. J., Broadhurst, T., & Illingworth, G. 2003a, *ApJ*, 593, 640
Bouwens, R. J., & Illingworth, G. D. 2005a, *NewA Rev.*, submitted (astro-ph/0510697)
Bouwens, R. J., Illingworth, G. D., Blakeslee, J. P., & Franx, M. 2006, *ApJ*, in press (astro-ph/0509641)
Bouwens, R. J., Illingworth, G. D., Thompson, R. I., & Franx, M. 2005b, *ApJ*, 624, L5
Bouwens, R. J., et al. 2003b, *ApJ*, 595, 589
———. 2004a, *ApJ*, 606, L25
———. 2004b, *ApJ*, 616, L79
Brinchmann, J., & Ellis, R. S. 2000, *ApJ*, 536, L77
Bruzual, G., & Charlot, S. 2003, *MNRAS*, 344, 1000
Buat, V., Boselli, A., Gavazzi, G., & Bonfanti, C. 2002, *A&A*, 383, 801
Buat, V., et al. 2005, *ApJ*, 619, L51
Bunker, A. J., Stanway, E. R., Ellis, R. S., & McMahon, R. G. 2004, *MNRAS*, 355, 374
Calura, F., & Matteucci, F. 2004, *MNRAS*, 350, 351
Calzetti, D. 2001, *PASP*, 113, 1449
Cappellaro, E., et al. 2005, *A&A*, 430, 83
Chary, R.-R., Stern, D., & Eisenhardt, P. 2005, *ApJ*, 635, L5
Cole, S., et al. 2001, *MNRAS*, 326, 255
Condon, J. J. 1992, *ARA&A*, 30, 575
Conti, A., et al. 2003, *AJ*, 126, 2330
Dahlen, T., et al. 2004, *ApJ*, 613, 189
Daigne, F., Olive, K. A., Sandick, P., & Vangioni, E. 2005, *Phys. Rev. D*, 72, 103007
Daigne, F., Olive, K. A., Vangioni-Flam, E., Silk, J., & Audouze, J. 2004, *ApJ*, 617, 693
Dickinson, M., Papovich, C., Ferguson, H. C., & Budavári, T. 2003, *ApJ*, 587, 25
Doherty, M., Bunker, A., Sharp, R., Dalton, G., Parry, I., & Lewis, I. 2006, *MNRAS*, 370, 331
Dunne, L., Eales, S. A., & Edmunds, M. G. 2003, *MNRAS*, 341, 589
Elmegreen, B. G., & Scalo, J. 2006, *ApJ*, 636, 149
Erb, D. K., Steidel, C. C., Shapley, A. E., Pettini, M., Reddy, N. A., & Adelberger, K. L. 2006, *ApJ*, in press (astro-ph/0604388)
Fardal, M. A., Katz, N., Weinberg, D. H., & Davé, R. 2006, *MNRAS*, submitted (astro-ph/0604534)
Fioc, M., & Rocca-Volmerange, B. 1997, *A&A*, 326, 950

- Förster, F., Wolf, C., Podsiadlowski, P., & Han, Z. 2006, *MNRAS*, 368, 1893
- Fukugita, M., & Kawasaki, M. 2003, *MNRAS*, 340, L7
- Giavalisco, M., et al. 2004, *ApJ*, 600, L103
- Granato, G. L., Lacey, C. G., Silva, L., Bressan, A., Baugh, C. M., Cole, S., & Frenk, C. S. 2000, *ApJ*, 542, 710
- Hanish, D. J., et al. 2006, *ApJ*, in press (astro-ph/0604442)
- Heavens, A., Panter, B., Jimenez, R., & Dunlop, J. 2004, *Nature*, 428, 625
- Heger, A., Fryer, C. L., Woosley, S. E., Langer, N., & Hartmann, D. H. 2003, *ApJ*, 591, 288
- Hogg, D. W., Cohen, J. G., Blandford, R., & Pahre, M. A. 1998, *ApJ*, 504, 622
- Hopkins, A. M. 2004, *ApJ*, 615, 209
- Hopkins, A. M., Connolly, A. J., Haarsma, D. B., & Cram, L. E. 2001, *AJ*, 122, 288
- Hopkins, A. M., Rao, S. M., & Turnshek, D. A. 2005, *ApJ*, 630, 108
- Hopkins, A. M., et al. 2003, *ApJ*, 599, 971
- Iglesias-Paramo, J., et al. 2006, *ApJS*, 164, 38
- Juneau, S., et al. 2005, *ApJ*, 619, L135
- Keil, M. T., Raffelt, G. G., & Janka, H. T. 2003, *ApJ*, 590, 971
- Kennicutt, R. C., Jr. 1983, *ApJ*, 272, 54
- . 1998, *ARA&A*, 36, 189
- Kennicutt, R. C., Jr., Tamblyn, P., & Congdon, C. E. 1994, *ApJ*, 435, 22
- Kroupa, P. 2001, *MNRAS*, 322, 231
- Le Fèvre, O., et al. 2005, *Nature*, 437, 519
- Le Floch, E., et al. 2005, *ApJ*, 632, 169
- Leitherer, C., et al. 1999, *ApJS*, 123, 3
- Liebendoerfer, M., Rampp, M., Janka, H. J., & Mezzacappa, A. 2005, *ApJ*, 620, 840
- Lilly, S. J., Le Fèvre, O., Hammer, F., & Crampton, D. 1996, *ApJ*, 460, L1
- Loewenstein, M. 2006, *ApJ*, in press (astro-ph/0605141)
- Lunardini, C. 2005, preprint (astro-ph/0509233)
- . 2006, *Phys. Rev. D*, 73, 083009
- Madau, P., della Valle, M., & Panagia, N. 1998, *MNRAS*, 297, L17
- Madau, P., Ferguson, H. C., Dickinson, M. E., Giavalisco, M., Steidel, C. C., & Fruchter, A. 1996, *MNRAS*, 283, 1388
- Malek, M., et al. 2003, *Phys. Rev. Lett.*, 90, 061101
- Mannucci, F., Della Valle, M., & Panagia, N. 2006, *MNRAS*, 370, 773
- Mannucci, F., et al. 2003, *A&A*, 401, 519
- Martin, D. C., et al. 2005, *ApJ*, 619, L59
- Mauch, T. 2005, Ph.D. thesis, Univ. of Sydney
- Maund, J. R., Smartt, S. J., & Danziger, I. J. 2005, *MNRAS*, 364, L33
- Menci, N., Cavaliere, A., Fontana, A., Giallongo, E., Poli, F., & Vittorini, V. 2004, *ApJ*, 604, 12
- Mesinger, A., Johnson, B. D., & Haiman, Z. 2006, *ApJ*, 637, 80
- Moustakas, J., Kennicutt, R. C., & Tremonti, C. A. 2006, *ApJ*, 642, 775
- Nagamine, K., Cen, R., Hernquist, L., Ostriker, J. P., & Springel, V. 2004, *ApJ*, 610, 45
- Neill, J. D., et al. 2006, *AJ*, 132, 1126
- Oda, T., & Totani, T. 2005, *ApJ*, 630, 59
- Ouchi, M., et al. 2004, *ApJ*, 611, 660
- Papovich, C., et al. 2006, *ApJ*, 640, 92
- Pei, Y. C., & Fall, S. M. 1995, *ApJ*, 454, 69
- Pérez-González, P. G., et al. 2005, *ApJ*, 630, 82
- Pinsonneault, M. H., & Stanek, K. Z. 2006, *ApJ*, 639, L67
- Raffelt, G. G. 1996, *Stars as Laboratories for Fundamental Physics: The Astrophysics of Neutrinos, Axions, and Other Weakly Interacting Particles* (Chicago: Univ. of Chicago Press)
- Rao, S. M., Turnshek, D. A., & Nestor, D. B. 2006, *ApJ*, 636, 610
- Renzini, A., & Voli, M. 1981, *A&A*, 94, 175
- Rudnick, G., et al. 2003, *ApJ*, 599, 847
- Salpeter, E. E. 1955, *ApJ*, 121, 161
- Scannapieco, E., & Bildsten, L. 2005, *ApJ*, 629, L85
- Schimminovich, D., et al. 2005, *ApJ*, 619, L47
- Smartt, S. J., Maund, J. R., Hendry, M. A., Tout, C. A., Gilmore, G. F., Mattila, S., & Benn, C. R. 2004, *Science*, 303, 499
- Somerville, R. S., Primack, J. R., & Faber, S. M. 2001, *MNRAS*, 320, 504
- Spergel, D. N., et al. 2003, *ApJS*, 148, 175
- Steidel, C. C., Adelberger, K. L., Giavalisco, M., Dickinson, M., & Pettini, M. 1999, *ApJ*, 519, 1
- Strigari, L. E., Beacom, J. F., Walker, T. P., & Zhang, P. 2005, *J. Cosmol. Astropart. Phys.*, 4, 17
- Strigari, L. E., Kaplinghat, M., Steigman, G., & Walker, T. P. 2004, *J. Cosmol. Astropart. Phys.*, 3, 7
- Strolger, L.-G., & Reiss, A. G. 2006, *AJ*, 131, 1629
- Sullivan, M., Mobasher, B., Chan, B., Cram, L., Ellis, R., Treyer, M., & Hopkins, A. 2001, *ApJ*, 558, 72
- Sumiyoshi, K., Yamada, S., Suzuki, H., Shen, H., Chiba, S., & Toki, H. 2005, *ApJ*, 629, 922
- Takeuchi, T. T., Buat, V., & Burgarella, D. 2005, *A&A*, 440, L17
- Thompson, R. I., Eisenstein, D., Fan, X., Dickinson, M., Illingworth, G., & Kennicutt, R. C. 2006, *ApJ*, 647, 787
- Thompson, T. A., Burrows, A., & Pinto, P. A. 2003, *ApJ*, 592, 434
- Van Dyk, S. D., Li, W., & Filippenko, A. V. 2006, *PASP*, 118, 351
- Vogel, P., & Beacom, J. F. 1999, *Phys. Rev. D*, 60, 053003
- Weidner, C., & Kroupa, P. 2005, *ApJ*, 625, 754
- . 2006, *MNRAS*, 365, 1333
- Wolf, C., Meisenheimer, K., Rix, H.-W., Borch, A., Dye, S., & Kleinheinrich, M. 2003, *A&A*, 401, 73
- Woosley, S. E., & Weaver, T. A. 1995, *ApJS*, 101, 181
- Yüksel, H., Ando, S., & Beacom, J. F. 2006, *Phys. Rev. C*, 74, 015803